RESEARCH ARTICLE

EcoMat FUNCTIONAL MATERIALS FOR GREEN ENERGY AND ENVIRONMENT **WILEY**

Simulation model of a non-contact triboelectric nanogenerator based on electrostatic induction

Jing You[1] | Jiajia Shao[2,3] | Yahua He[1] | Xin Guo[2,3] | K. W. See[1] |
Zhong Lin Wang[2,3] | Xiaolin Wang[1]

[1]Institute for Superconducting and Electronic Materials, Australian Institute for Innovative Materials, University of Wollongong, North Wollongong, New South Wales, Australia

[2]CAS Center for Excellence in Nanoscience, Beijing Key Laboratory of Micro-nano Energy and Sensor, Beijing Institute of Nanoenergy and Nanosystems, Chinese Academy of Sciences, Beijing, China

[3]College of Nanoscience and Technology, University of Chinese Academy of Sciences, Beijing, China

Correspondence
K. W. See and Xiaolin Wang, Institute for Superconducting and Electronic Materials, Australian Institute for Innovative Materials, University of Wollongong, North Wollongong, NSW 2500, Australia.
Email: kwsee@uow.edu.au and xiaolin@uow.edu.au

Abstract

Based on the coupling effects of contact electrification and electrostatic induction, a triboelectric nanogenerator (TENG) can convert mechanical energy into electric power, which is at the cutting edge of alternative energy technology. Although a considerable number of TENGs with different configurations have been designed, some of them however, which only depend on the electrostatic induction effect have not received enough attention. Here, a non-contact TENG model consists of copper rings and charged dielectric sphere is presented, which is aimed at exploring the working process of TENGs caused by electrostatic induction. Two classical models, including vertical and horizontal double copper rings models are also proposed. Relevant advanced and accurate models of TENGs have been established through the finite element method. We anticipate that the constructed model and theoretical analysis are helpful for the design of non-contact model TENGs with complicated geometric construction, and expand their applications in various fields.

KEYWORDS

COMSOL software, contact electrification, electrostatic induction, output characteristics, triboelectric nanogenerator

Jing You and Jiajia Shao contributed equally to this work.

1 | INTRODUCTION

Based on the coupling effects of contact electrification (CE) and electrostatic induction,[1–4] triboelectric nanogenerators (TENGs) have been fabricated and demonstrated as a cutting-edge technology in the field of energy conversion,[5–12] which belongs to the class of mechanical energy harvesters.[13–19] To date, four basic modes of TENGs have been designed, which are vertical contact mode, single-electrode mode, lateral sliding mode, and freestanding mode.[20] Each mode has its own respective structure and output characteristics. Using Maxwell's displacement current as the driving force,[21–24] a TENG device can effectively convert mechanical energy into electricity, giving TENGs many potential applications in our daily life, such as self-powered sensors, wearable electronics, raindrop energy collectors, etc.[25–32] A considerable number of TENGs with different configurations have been designed,[17,33–35] but most of them are operated according to the coupling effects of CE and electrostatic induction. Very few investigations have been carried out, however, for elucidating the working mechanism of TENGs that depend on electrostatic induction alone. In other words, this is an aspect that has not received enough attention in the past.

Zuankai Wang's group (2020) have developed a droplet-based electricity generator (DEG) to harvest energy from impinging water droplets, based on the effect of contact electrification and electrostatic induction.[36] The DEG utilizes a structure that includes an aluminum electrode and a polytetrafluoroethylene (PTFE) film atop an indium tin oxide (ITO) substrate. As the droplets continuously fall on the device, charges are generated and stored in the PTFE as a result of contact electrification between the water droplets and the fabricated device; while opposite charges are electrostatically induced on the ITO for charge transfer to the aluminum electrode, so a closed-loop electrical system is formed. Dating from 1867, one of the most remarkable and impressive displays of static electricity is an experiment using Lord Kelvin's water-drop electrostatic generator.[37–41] This classical device uses falling water to generate voltage differences by electrostatic induction occurring between interconnected, oppositely charged systems. The generated voltage keeps growing as the water droplets continue to impinge on the device, which eventually leads to an electric arc discharge in the form of a spark. This is a typical example of how electric power can be generated just through electrostatic induction. It should be noted that its simple construction makes this device popular in physics education as a laboratory experiment for students, which has been a big inspiration for us to design a special TENG device.

Here, inspired by Lord Kelvin's electrostatic water dropper, a copper-ring-model TENG has been designed, which consists of a charged dielectric sphere and two copper rings (Figure 1A). As a charged sphere passes through the center of the copper rings, opposite electrical charges are induced in the copper rings. Using this classical induction phenomenon, two types of models of TENGs have been constructed: a vertical double copper ring (metal electrode) model (VDR) and a horizontal double copper ring model (HDR). We have elaborated how the key parameters such as the radius of charged sphere and copper ring as well as the distances between the rings, etc., affect the basic output performance. Most importantly, the finite element method (FEM) through COMSOL software was utilized to simulate the whole energy harvesting system based on the TENGs. Despite the simple geometry of these structures, many interesting and surprising findings have been observed from the advanced simulations. For instance, some results indicate that the relative positions of the double copper rings sensitively influence the electric potentials of each ring. As the vertical distance between the two copper rings increases, the peak of electric potential begins to divide itself into two; but the two divided peaks are equal to each other. Through the established FEM models and the corresponding quantitative analysis, we expect to see these explorations help to characterize the output characteristics of TENGs, the operation of which only depends on the electrostatic induction, even when a non-contact model TENG device has an extremely complex and specific induced charge distribution.

Our research aims to provide significant insights into the operation of non-contact model triboelectric nanogenerators (TENGs) with a complex and spatially induced charge distribution. By gaining insights into the working mechanism of non-contact model TENGs, we can contribute to achieving optimal designs and applications of TENGs for efficient mechanical energy harvesting. The non-contact model TENGs could be more efficient, reliable, and cost-effective, allowing them to harness mechanical energy from various sources, including human motion, wind, and vibration, to power electronic devices. Overall, this research may provide reference information to drive the growth of sustainable energy harvesting technologies through not only by contact model TENGs but also by non-contact model TENGs.

2 | RESULTS AND DISCUSSION

As demonstrated in Figure 1A, a non-contact copper-ring model TENG consists of two parts: a charged dielectric
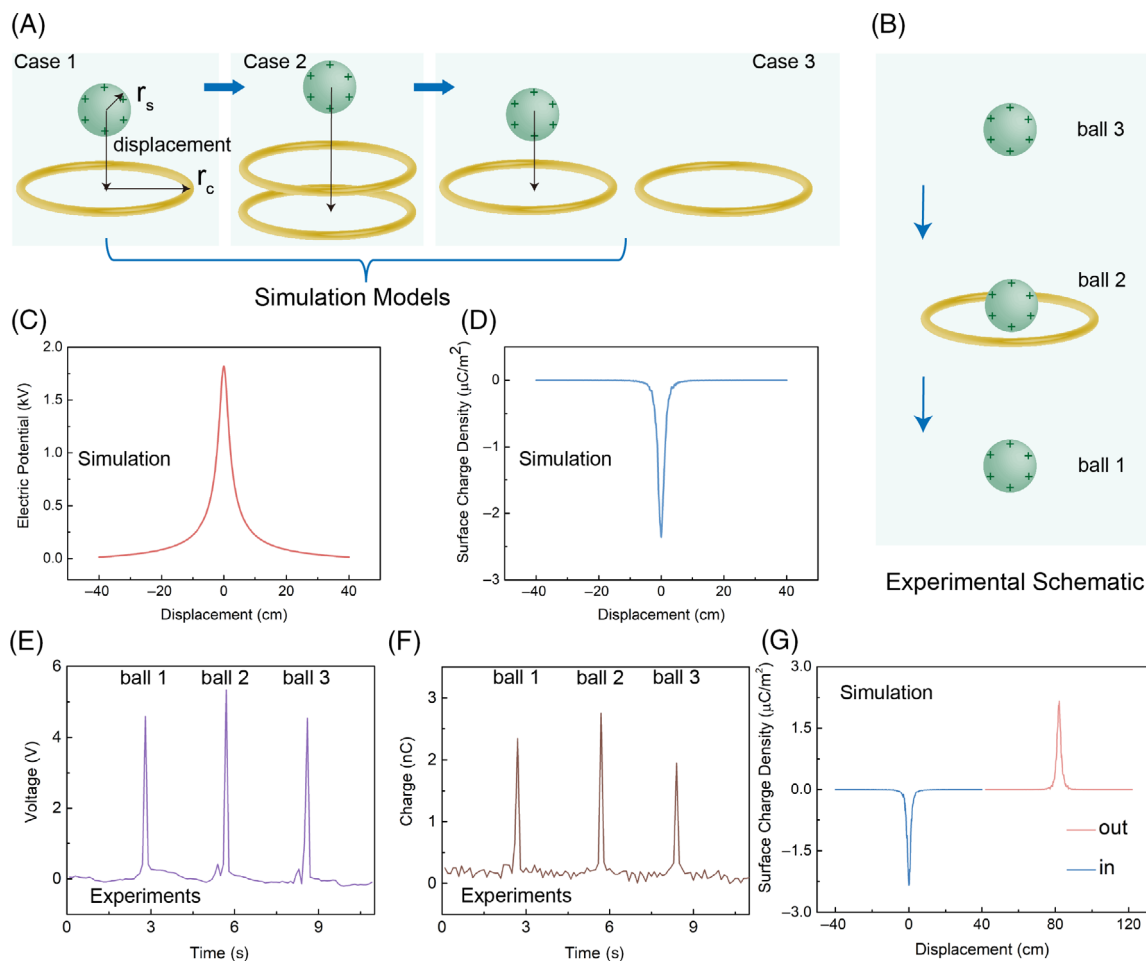
FIGURE 1 Schematic diagram showing the finite-element structure model, experimental schematic, and the comparison between the simulation results and experiments results. (A) Simulation model of charged sphere passing through a single copper ring, double vertical copper rings and double horizontal copper rings, respectively. (B) Experimental schematic of charged sphere passing through a single copper ring. The simulated (C, D) and experimental (E, F) electric potential and surface charge density of a single copper ring when a charged sphere passes through it (radius of charged sphere, $r_s = 0.5$ cm; radius of copper ring, $r_c = 1.5$ cm). (G) Surface charge density of inside and outside the copper ring when a positive charged sphere passed through.

sphere and two copper rings. As the charged dielectric sphere (moving part) passes through a copper ring, electric charges are induced and distributed on the surface of the copper ring. In particular, when the charged dielectric sphere is passed through the center of the copper ring, the largest electric potential and surface charge density are observed (Figure 1C,D). A series of experiments have been carried out to validate the simulation results, and the experimental schematic is demonstrated in Figure 1B. We have found that there is a good agreement between the experimental and simulation results. As illustrated in Figure 1E,F, three peaks are continuously produced when three positively charged spheres are passing through the copper ring. That is, it generates one peak at a time. Since the simulation model is proposed based on certain assumptions, such as assuming that the copper rings are perfect conductors and neglecting some

small effects that may occur in the experimental setup, there are some differences between the experimental and simulation results, which does not influence the accuracy of our conclusions.

It should be noticed that two opposite induced charge signals are obtained in Figure 1G (and Figure S1) when a positive charged sphere is passing through the copper ring. These seemingly paradoxical results can be explained through the effect of electrostatic induction. Electrostatic induction is a physical process, which leads to a redistribution of electric charge on one material under the influence of one or more nearby objects that have electric charge. When the positively charged dielectric sphere is brought near a copper ring (metal conductor, in Figure 1A), the positive charges start attracting the negative charges of the copper ring. Additionally, the positive charges repel the positive charges within the copper
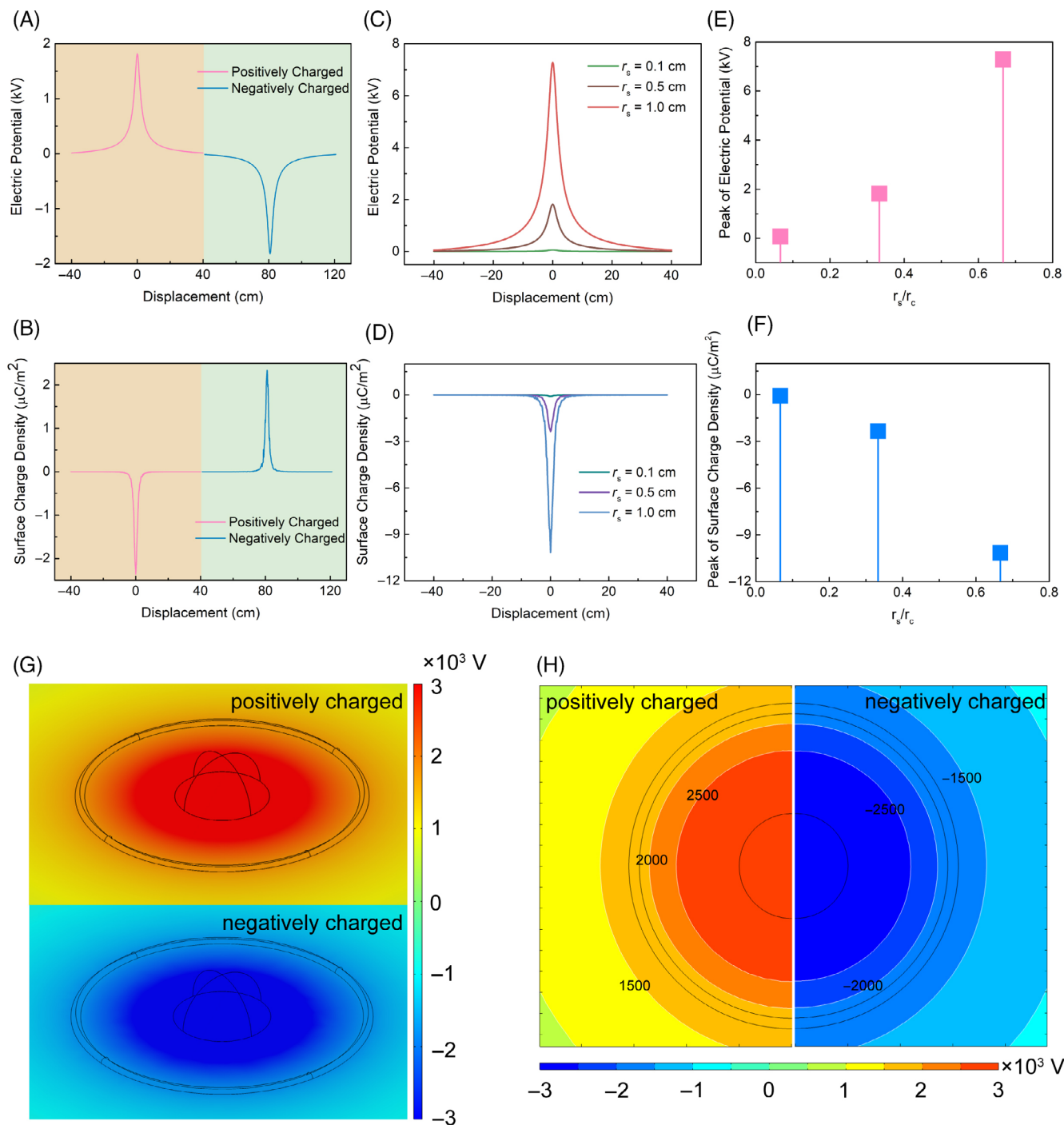
FIGURE 2 Basic simulation results for charged sphere passing through a single copper ring. (A) Electric potential and (B) surface charge density of the copper ring when a charged sphere passes through. (C–F) Electric potential and surface charge density of the copper ring when charged spheres with different radii pass through the charged sphere (the radius of the charged sphere, $r_s = 0.1$, 0.5, and 1.0 cm, while the radius of the copper ring, $r_c = 1.5$ cm). (G) Distribution of electric potential (V) and (H) its contours when the sphere is positively charged and negatively charged separately.

ring. This then creates a relocation of electrical charges within the metallic ring. That is why the induced negative charges and positive charges are located in and out of the copper ring, respectively (Figure 1G). Need to be reminded that in order to focus our attention to the

influence of electrostatic induction, the copper ring in our theoretical simulation model is no grounding. On the contrary, if the copper ring is grounded, only the opposite charges can be generated on the inside of the copper ring, because the like charges on the outside have been flowed
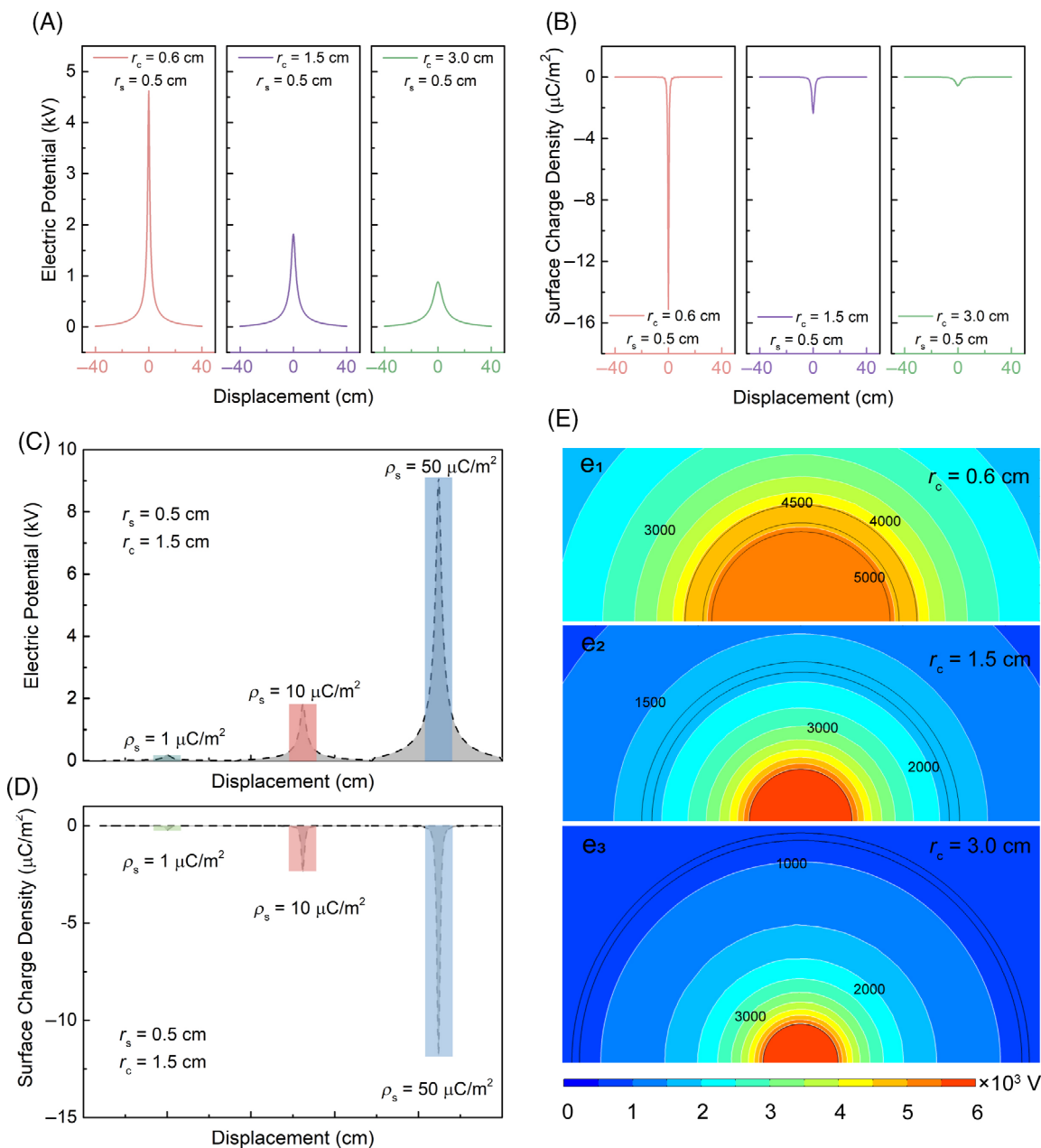
FIGURE 3 Simulation results for a charged sphere passing through single copper ring. (A) Electric potential and (B) surface charge density of the copper ring when a charged sphere passes through single copper rings with different radii ($r_s = 0.5$ cm, $r_c = 0.6$, 1.5, and 3.0 cm). (C) Electric potential and (D) surface charge density of the copper ring when charged spheres pass through with different charge densities ($r_s = 0.5$ cm, $r_c = 1.5$ cm, $\rho_s = 1$, 10, and 50 μC/m^2). (E) Contours of electric potential (V) when charged spheres ($\rho_s = 10$ μC/m2, $r_s = 0.5$ cm) pass through single copper rings with different radii ($r_c = 0.6$, 1.5, and 3.0 cm).

into the ground at this condition. Therefore, there is a positive charge signal is observed in Figure 1F. And in the experiments, the radii of the charged sphere (r_s), and copper ring (r_c) are 0.5 and 1.5 cm, respectively.

More simulations were performed to investigate what are the key influences and how these influences affect the electric potential and induced charge density. First, the influences of positively and negatively charged spheres were studied (Figure 2A,B). It is observed that a

positive electric potential signal is generated in the copper ring when a positively charged sphere passes through it, demonstrating the distribution of induced positive charges on the copper ring. In contrast, a negatively charged sphere passing through the copper ring results in a negative electric signal. The corresponding distributions of electric potential simulated by the FEM model are demonstrated in Figure 2G,H. It is well known that the geometry of the TENG structure exerts a strong influence

on the basic outputs. Here, we are first focusing on the radii of the charged sphere and the copper ring. Figure 2C reveals that there is a sharp rise of the electric potential when r_s is increased to 1.0 cm, while there is a marked drop as r_s is decreased to 0.5 cm. What can be clearly observed in Figure 2E is that the peak of the electric potential is proportional to the ratio of r_s/r_c. The electric potential peak reaches −7.28 kV when r_s/r_c is equal to 0.667, and it falls to −67 V as r_s/r_c decreases to 0.067. A similar phenomenon is shown in Figure 2D,F, where the peak of the induced surface charge density is proportional to the ratio of r_s/r_c as well. The simulation results depicted in Figure 2F show that the induced surface charge density peak grows to −10.157 μC/m^2 when r_s/r_c is 0.667, and it drops to −0.086 μC/m^2 as r_s/r_c decreases to 0.067.

We then changed the radius of copper ring r_c to validate the above findings. Figure 3A,B illustrates how the variation of r_c affects the electric potential and surface charge density of the copper ring, respectively. As the r_c increases from 0.6 cm to 3.0 cm, the electric potential of the copper ring decreases from 4.619 to 0.884 kV (Figure 3A), and the surface charge density exhibits a similar downward trend, which decreases from −15.117 to −0.566 μC/m^2 (Figure 3B). The electric potential contours calculated for different radii of the copper ring are illustrated in Figure 3E. These results further validate what is shown in Figure 2E,F. When the radius of the charged sphere is close to that of the copper ring (Figure 3E1), we can obtain a large electric potential and induced surface charge density in the copper ring. On the contrary, the reverse trend is seen if there is a bigger r_c (Figure 3E3). In addition, if the r_s and r_c remain constant but the surface charge density of the charged sphere varies, we can get some really interesting findings. The results presented in Figure 3C,D show that the electric potential and induced surface charge density are proportional to the surface charge density ρ_s of the charged sphere. When the ρ_s becomes gradually larger, from 1 to 50 μC/m^2, the electric potential of the copper ring is increased from 0.182 to 9.103 kV (Figure 3C,D); while the relevant induced surface charge density of the copper ring rises from 0.226 to 11.318 μC/m^2. Note that, since there is only one copper ring, this special structure can be regarded as a single mode TENG. So, we can reach the general conclusion that the basic output performance of this single mode TENG is strongly linked to the surface charge density of the charged sphere.

The above results are easily to understand and can be interpreted through electrostatics and the phenomenon of electrostatic induction. This electrostatic influence is a redistribution of electric charge on one material under the influence of one or more nearby objects that have

electric charge. The charged object acts through its electric field even to more distant bodies, thus changing their original non-electrical state. For instance, when a negatively charged dielectric sphere (charged object) is brought near a copper ring (metal conductor), the negative charges start attracting the positive charges of the copper ring. Additionally, the negative charges repel the negative charges within the copper ring. This then creates a relocation of electrical charges within the metallic ring. The electrical charges will remain in the redistributed state as long as the charged dielectric sphere is kept near the copper ring. When the charged sphere starts moving away, however, the metallic ring loses its charge instantaneously, which is because of the thermal motion of the atoms, which causes the charges to integrate again. Finally, an electric potential peak and induced surface charge peak are created.

Furthermore, when either the radius of the charged sphere or that of the copper ring (or both) increases/decreases, it will change the distance between them, changing the electric field intensity, which affects the charge redistribution of the copper ring. It should also be clear that the electric potential of the copper ring is determined by the special charge distributions in both the sphere and copper ring. In our simulations, the copper ring is never grounded, so the electrically charged sphere can induce equal and opposite charges in the copper ring (see Figure S1). When the charged sphere is either close to or far away from the copper ring, it does not receive or transfer any electrons from/to the copper ring (or metal electrode) by electrical induction., However, if the copper ring is grounded, charges opposite in polarity will become attracted according to the electrostatics; in other words, the copper ring will display the charge that is opposite to the inducing charge.

In addition, a vertical double copper ring model (VDR) was introduced to further investigate the variation of the output characteristic of a TENG based on electrostatic induction and to provide a thorough understanding of the charge distribution (Figure 1A). The VDR TENG model consists of a charged dielectric sphere (moving part, $r_s = 0.5$ cm) and double copper rings with the same radius ($r_c = 1.5$ cm). The double copper rings are vertically oriented and centered on the same y axis. As the charged dielectric sphere passes through the two copper rings successively, electric charges are induced and distributed on the surfaces of both of the copper rings. We have investigated the influence of geometrical parameters in the single copper ring model, such as the radius of the charged sphere and copper ring; here we are focusing on the vertical distance between the vertical double copper rings. Under open circuit (OC) conditions, no charges are transferred between the two copper rings, and
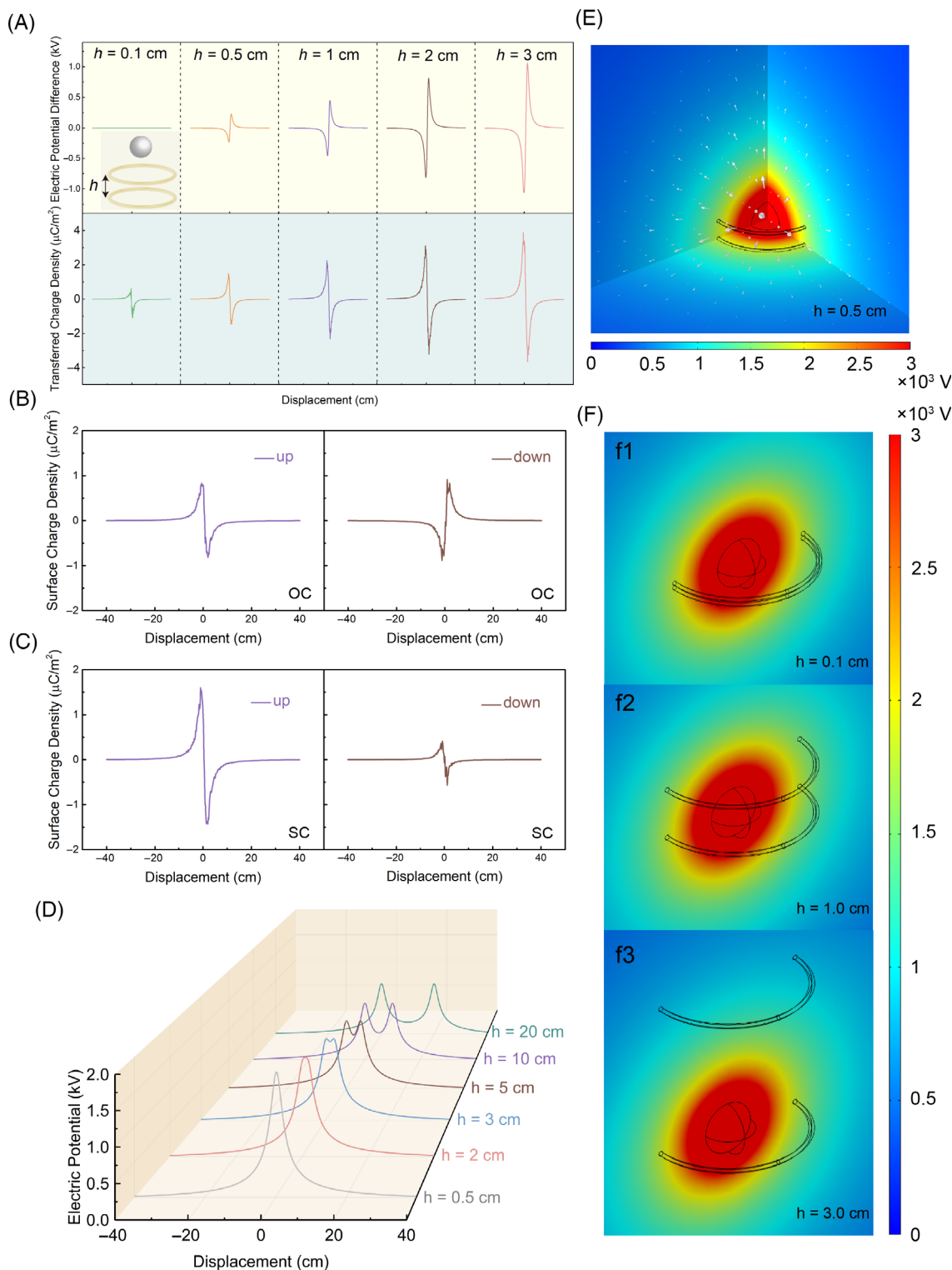
FIGURE 4 Simulation results for a charged sphere passing through vertical double copper rings ($\rho_s = 10$ μC/m2, $r_s = 0.5$ cm, with the radius of the double vertical copper rings the same, $r_c = 1.5$ cm). (A) Electric potential difference (in the open-circuit condition) and transferred charge density (in the short-circuit condition) between double vertical copper rings when a charged sphere pass through at different heights of the top ring (where the height between the double vertical copper rings, $h = 0.1, 0.5, 1, 2$, and 3 cm). Surface charge density of different positions on the copper ring under (B) open-circuit (OC) conditions and (C) short-circuit (SC) conditions. (D) Electric potential of vertical double rings in the OC condition when h changes ($h = 0.5, 2, 3, 5, 10$, and 20 cm). (E) Three-dimensional distribution of electric potential (indicated by colors) and electric field (indicated by arrows) when a charged sphere pass through the double vertical copper rings separated by 0.5 cm. (F) Distribution of electric potential under OC conditions when h changes ($h = 0.1, 1.0$, and 3.0 cm).

consequently, only induced electric charges are distributed on the surfaces of the copper rings, so the electric potential difference between the double copper rings is presented. Under short-circuit (SC) conditions, free charges flow in the double copper rings to reduce the potential difference, so the transferred charged density of the double copper rings is presented. The electric potential difference at OC condition and the transferred charge density at SC condition between double copper rings with different vertical separations (heights) are presented in Figure 4A. It can be easily observed that the open circuit voltage and transferred charge density are proportional to the vertical distance, illustrating that the relative distance sensitively affects the output performance of the VDR TENG model. Several other intriguing findings have been found also, such as the fact that the surface charge density varies significantly among the various positions of the copper ring (Figure 4B,C). The surface charge density at the two points of the vertical double copper rings has a similar value but a different trend while they are operating under OC conditions. On the other hand, the surface charge density of both points shows the same trend but a different value when the vertical double copper rings are under SC conditions. The above mentioned phenomena are attributed to the symmetrical structure of the double copper rings. When the charged dielectric sphere passes through the center of the copper ring, it induces equal and opposite charges on both sides of the copper ring due to the symmetry. Note that because the double copper rings whether at OC or SC conditions are not grounded, the similar surface charge density can be obtained. In theory, the surface charge densities at any point in the copper rings should be same at SC conditions, since it must keep the same electrical potential of the two copper rings. However, the copper rings have no grounding in our simulations, which make the free charges distributed in these rings cannot flow freely, thus generating a non-uniform surface charge density. But what is certain is that the total charges stay the same. This is the reason why there are different peak shapes of the up and down in Figure 1C.

Figure 4D presents the electric potential of both copper rings under SC conditions. The electric potential of each copper ring in the VDR model drops with increasing vertical separation. The peak electric potential of double copper rings at 0.5 cm in height is 1.787 kV, which is comparable to the basic output of the single copper ring model (1.82 kV). The peak value only reaches 0.949 kV when the height is 20 cm. Another finding is that when the vertical separation is large enough (in this case, 3 cm), the peak of the electric potential is divided into two, and the two newly formed peaks are equal to one another while maintaining symmetry. This phenomenon

indicates that as the vertical separation increases, the effect of induced electrification caused by one copper ring enhances gradually, which generates peak one by one when the charged sphere passing through.

When the charged dielectric sphere approaches the open-circuited double copper rings, the free electrons in the ring experience a static electric force and move to the area farther away from the charged sphere, leading to the creation of induced charges on the ring. These induced charges create an electric field and induce an electric potential. The magnitude of the induced potential depends on the distribution and variation of the electric field. When the charged sphere passes through the copper rings vertically, the induced charges concentrate at the top and bottom of the vertical double copper ring model, creating an electric potential and inducing an electric current on the ring. As the vertical separation increases, the electric field lines generated by the two copper rings become more diffused, and the total strength of the electric field decreases, either, which generates a lower electric potential. Most importantly, when the vertical separation increases to some extent ($h = 5$ cm), the time difference through the copper ring plays an increasingly important role, thus generating peaks one by one and each corresponding to the induction effect of a single copper ring. So, this is in fact a revelation to us that an appropriate architecture is strongly important for a non-contact model TENG. Figure 4E demonstrates the three-dimensional distributions of electric potential and electric field (arrows) when the charged dielectric sphere is passing through the center of the copper rings. The electric potential contours calculated at different vertical distances of the double copper rings are described in Figure 4F, which directly depicts the effect of the vertical separation of the rings on the output performance of the VDR model.

Moreover, the VDR model was converted to an offset double-copper-ring model (with horizontal as well as vertical separation of the centers of the rings) to validate the above findings. A schematic illustration of a charged sphere passing through the offset double rings model is presented in Figure 5C with its key parameters attached. Here, the horizontal distance s between the centers of double copper rings is treated as the most important factor in the model, and the investigation covered the situations where both double copper rings were at OC condition and where they were at SC condition. The electric potential difference between the double copper rings in the OC condition is shown in detail according to the variation of s in Figure 5A. It can be clearly seen that the electric potential difference grows with s, and what is also interestingly found is that two electric potential peaks are first created, and then they merge into a single
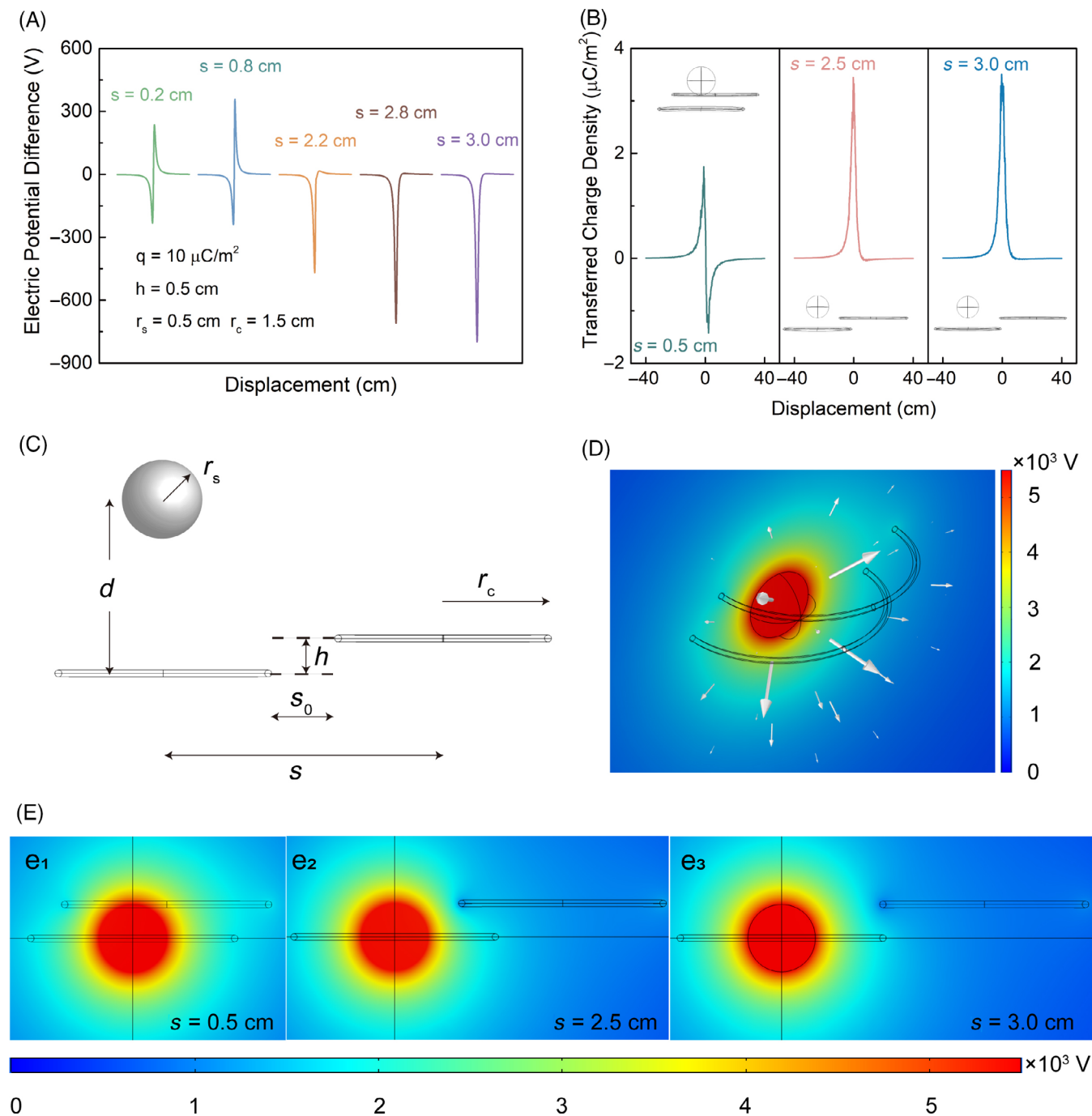
FIGURE 5 Simulation results for a charged sphere passing through offset double copper rings ($\rho_s = 10\ \mu C/m^2$, $r_s = 0.5$ cm, with the radii of the double vertical copper rings the same, $r_c = 1.5$ cm). (A) Electric potential difference between double offset copper rings in the OC condition when the charged sphere passes through at different horizontal offsets s ($s = 0.2, 0.8, 2.2, 2.8$, and 3.0 cm). (B) Transferred charge density between double offset copper rings in the SC condition when s changes ($s = 0.5, 2.5$, and 3.0 cm). (C) Structure of charged sphere passing through double copper rings and relevant parameters. The variables in the structure are defined as follows: r_s represents the radius of the charged dielectric sphere, r_c represents the radius of both copper rings, d represents the displacement of the sphere, h represents the vertical height between the double copper rings, S_0 represents the minimum horizontal distance between the double copper rings, and S represents the horizontal distance between the center of the double copper rings. (D) Three-dimensional distribution of electric potential (colors) and electric field (arrows) when the charged sphere passes through the offset vertical copper rings horizontal offset of 0.5 cm. (E) Distribution of electric potential in the OC conditions when s changes ($s = 0.5, 2.5$, and 3.0 cm).
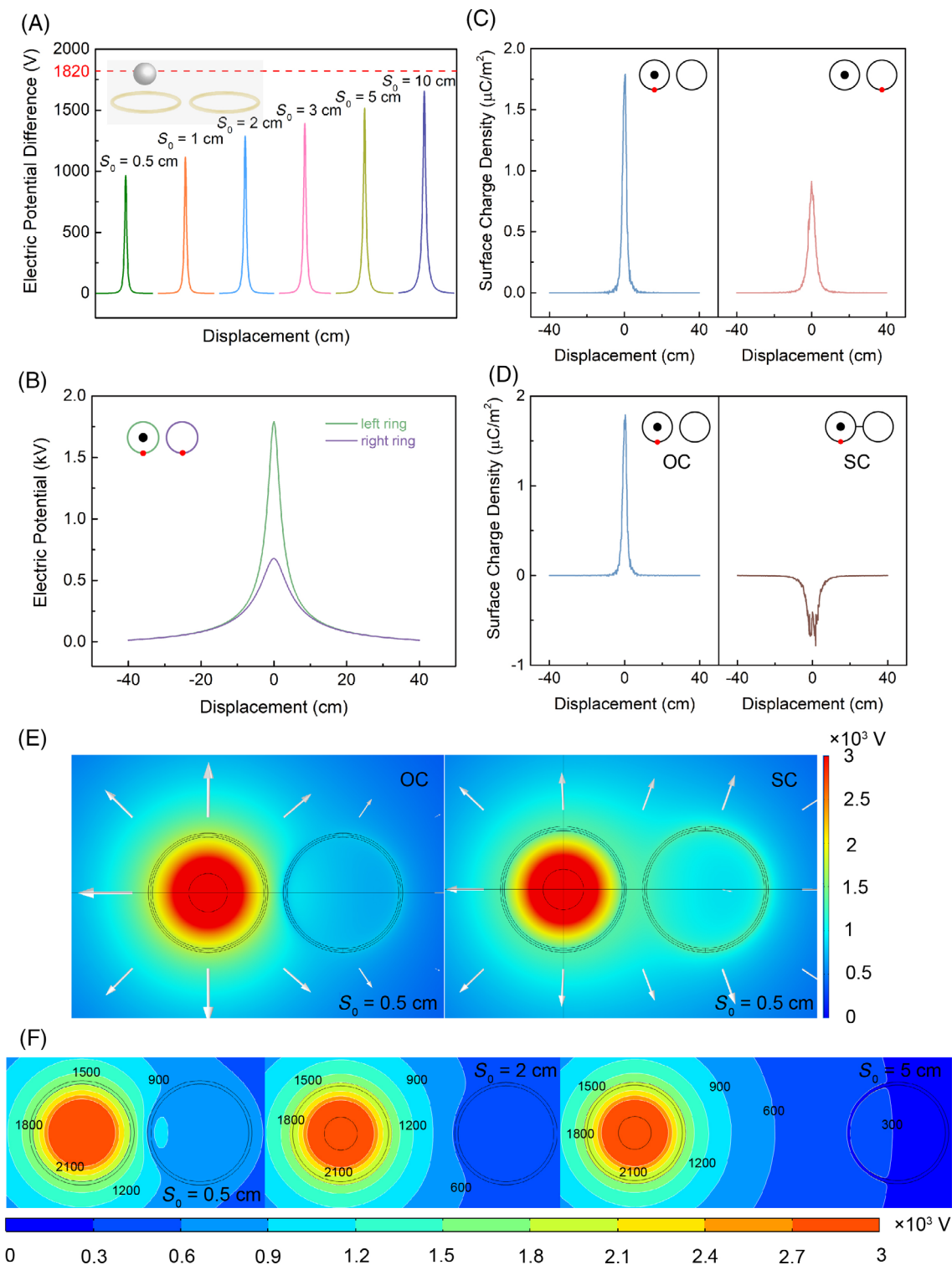
FIGURE 6 Simulation results of charged sphere passing through horizontal double copper rings ($\rho_s = 10$ μC/m², $r_s = 0.5$ cm, the radii of the double horizontal copper rings are the same, $r_c = 1.5$ cm). (A) Electric potential difference between double horizontal copper rings when the closest distance between the double horizontal copper rings S_0 changes ($S_0 = 0.5, 1, 2, 3, 5,$ and 10 cm). (B) Electric potential and (C) surface charge density of both horizontal copper rings under OC conditions when $S_0 = 0.5$ cm. (D) Surface charge density comparison when the horizontal double copper rings are under OC and SC conditions. (E) Distribution of electric potential (colors) and electric field (arrows) when the charged sphere passes through the double horizontal copper rings. (F) Contours of the electric potential (V) under OC conditions when the distance between the double horizontal copper rings S_0 changes ($S_0 = 0.5$ cm, 2 cm, and 5 cm).

peak as the horizontal distance between the centers of the copper rings varies from 0.8 to 2.2 cm. The same phenomenon is also exhibited for the peak of transferred charge density at SC condition (Figure 5B). Figure 5E shows slices of the electric potential distribution when the charged dielectric sphere is at the center of the lower copper ring (with the double copper rings at OC condition), which validates the above results again. A three-dimensional electric potential distribution of the offset double-copper-ring model at SC condition is given in Figure 5D, with the arrows representing the electric field and the charged sphere at the center of the lower copper ring at a distance s of 0.5 cm. Note that, we fixed the radius of the charged sphere r_s, the radius of both copper rings r_c, the surface charge density of the sphere, and the vertical height between the double copper rings h at 0.5 cm, 1.5 cm, 10 $\mu C/m^2$, and 0.5 cm, respectively, in the offset double copper rings model.

Whether the two created peaks merged into one single peak for the offset double-copper-ring model, or the one single peak derived into two equal and symmetry peaks of the vertical double copper ring model, the essential reason of generating above two phenomena is the same, both of which are caused by electrostatic induction. When the positions of the two copper rings are strongly close to each other, the induced charges can be created at about the same time, giving rise to the generation of one electric potential peak (Figure 4). For the offset double-copper-ring model, if the distance s is small enough, such as when it is equal to 0.2 cm, the charged sphere can pass through the two copper rings instantaneously and simultaneously. That is why two peaks of electric potential and surface charge density has been observed; in other words, the geometry structure of the VDR model is similar to that of the offset double-copper-ring model. However, as the distance of s increases until it is sufficiently large (for instance, $s = 2.2$ cm), two copper rings (partitions) cannot interfere with each other (Figure S2). As a result, the charged sphere just passes one copper ring each time, and only one single peak is observed. On the other hand, through the positions of the two electric potential or transferred charges peaks, one can design and fabricate a special kind of position sensors to detect the moving objects in practice.

Finally, the HDR model was constructed to illustrate whether interaction effects occur between the two copper rings. Two copper rings are placed on the same horizontal plane, while the charged dielectric sphere passes through the left copper ring only. Here, the key factor is the minimum distance S_0 between the horizontal double copper rings (Figure 5C), and the output performance of the HDR models were investigated under both OC and

SC conditions. Under OC conditions, it can be clearly seen from Figure 6A that the open circuit voltage between the double copper rings increases proportionally with S_0. Figure 6B presents the electric potential of both the horizontal copper rings in detail, respectively (outputs of different distances are presented in Figures S2 and S3). It should be noted that the electric potential of the left copper ring that charged dielectric sphere passes through is constant at 1820 V, which is same as the output in the single-copper-ring model. Since the distance between the charged sphere and the left copper ring remains constant, there is no variation of the electric field intensity, which means that the charge redistribution of the left copper ring remains constant. The variation of the horizontal distance S_0 affects the charges redistribution of the right copper ring, thus affecting the open circuit voltage between double copper rings.

Although there is no charge transfer between the copper rings when they are under OC conditions, the surface charge densities of both copper rings (Figure 6C) at the minimum distance S_0 of 0.5 cm are different with each other. We find that the surface charge density of the left copper ring where the charged sphere passes through is obviously larger than that of the right copper ring, which is mainly because the left copper ring is closer to the charged body. To keep the process of electrostatic equilibrium, large number of charges are induced rapidly in this copper ring, resulting a higher peak than that of the right copper ring. The contours of the double copper rings under OC conditions when S_0 is changed are depicted in Figure 6F, which obviously demonstrates the variation of electric potential when S_0 is varied from 0.5 to 3.0 cm. The output performance was also simulated for the situation where the double horizontal copper rings are under SC conditions, and the results were compared with those under OC conditions at the distance S_0 of 0.5 cm. The surface charge density of the left copper ring that the charged sphere passes through is given in Figure 6D under both OC and SC conditions. The electric potentials under both conditions are compared in Figure 6E with the arrows representing the electric field. From the above findings, we can reach the general conclusion that the relative distances and positions of the double copper rings extraordinarily affect the basic output performances of HDR TENG models. The detailed reason about why these phenomena has been happened were mentioned above.

3 | CONCLUSION

Inspired by Lord Kelvin's water-drop electrostatic generator, non-contact copper ring TENGs, including vertical

and horizontal models are developed in this work, which are intended to harvest mechanical energy only through the effect of electrostatic induction. By using COMSOL, the large finite element method software package, we have explained how different key parameters, such as the size of the charged sphere and copper ring, the surface charge density, and the relative positions of the copper rings, affect and control the basic output performance of TENGs. It was observed that the electric potential and induced surface charge density are proportional to the radius of the charged sphere, and interestingly they are inversely proportional to the radius of copper ring. What needs to be emphasized is that the electric potential and transferred charges of the designed TENGs are powerfully influenced by the relative positions of these copper rings.

In the case of the vertical double copper ring (VDR) model TENG, its open circuit voltage is proportional to the vertical distance between the two copper rings. Under short circuit conditions, however, the electric potential of each copper ring decreases with increasing vertical spacing. When the vertical spacing was large enough (for instance, 3 cm in this work), the peak of the electric potential began to divide itself into two; and the two generated two peaks were equal to each other, always maintaining symmetry. In the case of the horizontal double copper ring (HDR) model TENG, it is interestingly found that the two electric potential peaks are created first, and they then merge into one peak as the distances between the copper rings increases from 0.2 cm to 2.2 cm. The same phenomenon was also exhibited by the peak of the transferred charge density for the HDR model TENG. The non-contact copper ring model TENG is chiefly characterized by the simplicity of its structure, but it could exhibit enough information to describe the basic output characteristics of TENGs that harvests energy just by the electrostatic induction effect alone. This work is likely to provide special insights to understand the working mechanism of non-contact model TENGs with a complex and spatially induced charge distribution, thus contributing to the achievement of optimum designs and applications of TENGs for mechanical energy harvesting.

4 | METHODS

The simulations were carried out through the COMSOL Multiphysics software, version 5.6. In this work, a quasistatic model is built to simulate the electrostatic induction between a dielectric sphere and the copper rings, using the AC/DC module from COMSOL. The dielectric constant of the dielectric sphere is 4.4, and the copper rings were modeled as perfect conductors with a conductivity of 5.998×10^7 S/m. The detailed geometric parameters of the copper rings and dielectric sphere are set based on the experimental setup, which are given in supplementary information. Moreover, subject to the single-copper-ring model, the total surface charge on the copper ring was set to 0. For the double-copper-ring models, the total surface charges on each copper ring were set to 0 under OC conditions, while the potentials of the two copper rings were equal to each other under SC boundary conditions. The output characteristics were numerically evaluated by solving the governing equation. After exactly determining the charge distribution in a TENG device, the electric potential and surface charge distribution were investigated with detailed numerical simulations. The COMSOL environment parameters that were tested are summarized in Tables S1–S3.

CONFLICT OF INTEREST STATEMENT

The authors declare no conflict of interest.

ORCID

Zhong Lin Wang https://orcid.org/0000-0002-5530-0380
Xiaolin Wang https://orcid.org/0000-0003-4150-0848

REFERENCES

1. Wang ZL. From contact electrification to triboelectric nanogenerators. *Rep Prog Phys*. 2021;84(9):096502. doi:10.1088/1361-6633/ac0a50

2. Wang ZL, Wang AC. On the origin of contact-electrification. *Mater Today*. 2019;30:34-51. doi:10.1016/j.mattod

3. Kaponig M, Mölleken A, Nienhaus H, Möller R. Dynamics of contact electrification. *Sci Adv*. 2021;7(22):eabg7595. doi:10.1126/sciadv.abg7595

4. Nie J, Ren Z, Xu L, et al. Probing contact-electrification-induced electron and ion transfers at a liquid-solid Interface. *Adv Mater*. 2020;32(2):e1905696. doi:10.1002/adma.201905696

5. Hinchet R, Yoon H, Ryu H, et al. Transcutaneous ultrasound energy harvesting using capacitive triboelectric technology. *Science*. 2019;365(6452):491-494. doi:10.1126/science.an3997

6. Kim J, Cho H, Han M, et al. Ultrahigh power output from triboelectric Nanogenerator based on serrated electrode via spark discharge. *Adv Energy Mater*. 2020;10(44):2002312. doi:10.1002/aenm.202002312

7. Wang ZL. Triboelectric Nanogenerator (TENG)—sparking an energy and sensor revolution. *Adv Energy Mater*. 2020;10(17):2000137. doi:10.1002/aenm.202000137

8. Wang ZL, Jiang T, Xu L. Toward the blue energy dream by triboelectric nanogenerator networks. *Nano Energy*. 2017;39:9-23. doi:10.1016/j.nanoen.2017.06.035

9. You J, Shao J, He Y, et al. High-electrification performance and mechanism of a water-solid mode triboelectric Nanogenerator. *ACS Nano*. 2021;15(5):8706-8714. doi:10.1021/acsnano.1c00795

10. Huang L, Lin S, Xu Z, et al. Fiber-based energy conversion devices for human-body energy harvesting. *Adv Mater*. 2020;32(5):e1902034. doi:10.1002/adma.201902034

11. Shao J, Yang Y, Yang O, Wang J, Willatzen M, Wang ZL. Designing rules and optimization of triboelectric Nanogenerator arrays. *Adv Energy Mater*. 2021;11(16):2100065. doi:10.1002/aenm.202100065

12. Shao J, Willatzen M, Shi Y, Wang ZL. 3D mathematical model of contact-separation and single-electrode mode triboelectric nanogenerators. *Nano Energy*. 2019;60:630-640. doi:10.1016/j.nanoen.2019.03.072

13. Qin H, Xu L, Lin S, et al. Underwater energy harvesting and sensing by sweeping out the charges in an electric double layer using an oil droplet. *Adv Funct Mater*. 2022;32(18):2111662. doi:10.1002/adfm.202111662

14. Wu H, Mendel N, van den Ende D, Zhou G, Mugele F. Energy harvesting from drops impacting onto charged surfaces. *Phys Rev Lett*. 2020;125(7):078301. doi:10.1103/PhysRevLett.125.078301

15. Zhao X, Kuang S, Wang ZL, Zhu G. Highly adaptive solid-liquid interfacing triboelectric Nanogenerator for harvesting diverse water wave energy. *ACS Nano*. 2018;12(5):4280-4285. doi:10.1021/acsnano.7b08716

16. Su Y, Wen X, Zhu G, et al. Hybrid triboelectric nanogenerator for harvesting water wave energy and as a self-powered distress signal emitter. *Nano Energy*. 2014;9:186-195. doi:10.1016/j.nanoen.2014.07.006

17. Vallem V, Roosa E, Ledinh T, et al. A soft variable-area electrical-double-layer energy harvester. *Adv Mater*. 2021;33(43):e2103142. doi:10.1002/adma.202103142

18. Liang X, Jiang T, Liu G, et al. Triboelectric Nanogenerator networks integrated with power management module for water wave energy harvesting. *Adv Funct Mater*. 2019;29(41):1807241. doi:10.1002/adfm.201807241

19. Wang J, Wu C, Dai Y, et al. Achieving ultrahigh triboelectric charge density for efficient energy harvesting. *Nat Commun*. 2017;8(1):88. doi:10.1038/s41467-017-00131-4

20. Niu S, Wang ZL. Theoretical systems of triboelectric nanogenerators. *Nano Energy*. 2015;14:161-192. doi:10.1016/j.nanoen.2014.11.034

21. Wang ZL. On the expanded Maxwell's equations for moving charged media system – general theory, mathematical solutions and applications in TENG. *Mater Today*. 2021;52:348-363. doi:10.1016/j.mattod.2021.10.027

22. Wang ZL. On the first principle theory of nanogenerators from Maxwell's equations. *Nano Energy*. 2019;68:104272. doi:10.1016/j.nanoen.2019.104272

23. Shao J, Willatzen M, Jiang T, et al. Quantifying the power output and structural figure-of-merits of triboelectric nanogenerators in a charging system starting from the Maxwell's displacement current. *Nano Energy*. 2019;59:380-389. doi:10.1016/j.nanoen.2019.02.051

24. Wang ZL. On Maxwell's displacement current for energy and sensors: the origin of nanogenerators. *Mater Today*. 2017;20(2):74-82. doi:10.1016/j.mattod.2016.12.001

25. Ryu H, Park HM, Kim MK, et al. Self-rechargeable cardiac pacemaker system with triboelectric nanogenerators. *Nat Commun*. 2021;12(1):4374. doi:10.1038/s41467-021-24417-w

26. Han SA, Seung W, Kim JH, Kim S-W. Ultrathin noncontact-mode triboelectric Nanogenerator triggered by Giant dielectric material adaption. *ACS Energy Lett*. 2021;6(4):1189-1197. doi:10.1021/acsenergylett.0c02434

27. Huo ZY, Lee DM, Jeong JM, et al. Microbial disinfection with supercoiling capacitive triboelectric Nanogenerator. *Adv Energy Mater*. 2022;12(15):2103680. doi:10.1002/aenm.202103680

28. Yang Y, Sun N, Wen Z, et al. Liquid-metal-based super-stretchable and structure-designable triboelectric Nanogenerator for wearable electronics. *ACS Nano*. 2018;12(2):2027-2034. doi:10.1021/acsnano.8b00147

29. Dong K, Peng X, Wang ZL. Fiber/fabric-based piezoelectric and triboelectric Nanogenerators for flexible/stretchable and wearable electronics and artificial intelligence. *Adv Mater*. 2020;32(5):e1902549. doi:10.1002/adma.201902549

30. Li Z, Yang D, Zhang Z, et al. A droplet-based electricity generator for large-scale raindrop energy harvesting. *Nano Energy*. 2022;100:100. doi:10.1016/j.nanoen.2022.107443

31. Lee D, Rubab N, Hyun I, et al. Ultrasound-mediated triboelectric nanogenerator for powering on-demand transient electronics. *Sci Adv*. 2022;8:eabl8423. doi:10.1126/sciadv.abl8423

32. Meng X, Xiao X, Jeon S, et al. An ultrasound-driven bioadhesive triboelectric Nanogenerator for instant wound sealing and electrically accelerated healing in emergencies. *Adv Mater*. 2023;35(12):e2209054. doi:10.1002/adma.202209054

33. Guo X, Shao J, Willatzen M, Yang Y, Wang ZL. Theoretical model and optimal output of a cylindrical triboelectric nanogenerator. *Nano Energy*. 2022;92:92. doi:10.1016/j.nanoen.2021.106762

34. Gravesen J, Willatzen M, Shao J, Wang ZL. Energy optimization of a mirror-symmetric spherical triboelectric nanogenerator. *Adv Funct Mater*. 2022;32(18):2110516. doi:10.1002/adfm.202110516

35. Zhang N, Zhang H, Xu W, et al. A droplet-based electricity generator with ultrahigh instantaneous output and short charging time. *Droplet*. 2022;1(1):56-64. doi:10.1002/dro2.10

36. Xu W, Zheng H, Liu Y, et al. A droplet-based electricity generator with high instantaneous power density. *Nature*. 2020; 578(7795):392-396. doi:10.1038/s41586-020-1985-6

37. Sutton R, ed. *Demonstration Experiments in Physics*. New York: McGraw-Hill; 1938:261-262.

38. Lloyd JT. Lord Kelvin demonstrated. *Phys Teach*. 1980;18(1): 16-24. doi:10.1119/1.2340402

39. Evans L, Stevens JT. Kelvin water dropper revisited. *Phys Teach*. 1977;15(9):548-549. doi:10.1119/1.2339770

40. Sady M. The kelvin water dropper: an elementary experience. *Phys Teach*. 1984;22(8):516. doi:10.1119/1.2341642

41. Mak S-y. The kelvin water-drop electrostatic generator—an improved design. *Phys Teach*. 1997;35(9):549-551. doi:10.1119/1.2344804

SUPPORTING INFORMATION

Additional supporting information can be found online in the Supporting Information section at the end of this article.

How to cite this article: You J, Shao J, He Y, et al. Simulation model of a non-contact triboelectric nanogenerator based on electrostatic induction. *EcoMat*. 2023;e12392. doi:10.1002/eom2.12392